Materials Advances

ROYAL SOCIETY OF CHEMISTRY

PAPER

View Article Online
View Journal

Cite this: DOI: 10.1039/d6ma00091f

Synergistic *Tamra-Yasad Bhasma* and cinnamaldehyde nano-shield hydrogels for diabetic wound repair

Suhela Tyeb, *[a] Nitesh Kumar,[b] Vivek Verma,[c] Ashok Kumar[d] and Sanjana Kaul[a]

Received 21st January 2026,
Accepted 3rd April 2026

DOI: 10.1039/d6ma00091f

rsc.li/materials-advances

Around 100 million individuals with diabetes in India are at risk of developing diabetic wounds in their lifetime. These wounds cause severe reductions in the quality of life of patients due to increased economic burden and risk of limb amputations. Indigenous wound dressings offer cost-effective solutions for the management and healing of such wounds. Loading of bioactive formulations in passive dressing material has led to successful intervention in hampered wound healing cascades. The role of traditional wound healing formulations, such as aloe vera, turmeric, and cinnamon oil extracts loaded in hydrogels, hydrocolloids, sponges and other dressing materials, has been reported earlier. *Tamra Bhasma* and *Yasad Bhasma* are two types of Ayurvedic formulations (Bhasmas) cited in the Indian traditional medicinal text "Rasa-shastra". These Bhasmas have been studied in isolation and show beneficial attributes, such as free radical scavenging, hepatoprotective activity and anti-inflammatory effects. The present work is aimed at studying the combinatorial effect of *Tamra Bhasma* and *Yasad Bhasma* in conjunction with the potent anti-microbial "cinnamaldehyde nanoemulsion (NE)" loaded in two different forms of a polyvinyl alcohol (PVA) matrix: hydrogel and sponge. *In vitro* studies on three cell lines, NIH 3T3, HaCaT and HuVECs, showed sustained release of these Bhasmas and NE, leading to enhanced cell proliferation, cell migration, free radical scavenging and collagen formation. Compared with the PVA hydrogel and sponge controls, the developed bioactive wound dressing shows promise for the healing and management of infected diabetic wounds.

1. Introduction

Diabetic wounds are difficult to heal owing to hampered angiogenesis, risk of infection and impaired collagen formation. Multiple interventions have been examined in previous studies on biochemical pathways, addressing different phases of the wound-healing cascade. In this regard, hydrogels, hydrocolloids and sponges loaded with growth factors, debriding agents, antibiotics, exosomes and metallic nanoparticles have been explored.[1] Hydrogels are a class of water-soluble polymers with tunable properties, such as swelling, water–vapor transmission, porosity, stiffness and non-immunogenicity, that are suitable for dermal and epidermal wound healing.[2,3] Polyvinyl alcohol (PVA) is one such hydrogel polymer that has been used extensively for the healing and management of chronic diabetic wounds.[4,5] Bialik-wqs *et al.* synthesized PVA-sodium alginate (SA) composite hydrogels for the prolonged release of aloe vera as a promising wound-healing material.[6] Wang *et al.* developed a piezoelectric PVA-PVDF-based composite hydrogel to enhance the cellular proliferation, migration and secretion of ECM proteins for efficient healing of chronic wounds.[7] Some of the earlier works studied the release of traditional medicines from PVA hydrogel matrices, such as that reported by Wang *et al.*[8] The authors prepared a PVA-chitosan composite hydrogel for the sustained release of the Tibetan eighteen flavor dangshen pills to promote the anti-inflammatory, cell proliferative and analgesic properties of the Tibetan medicine for chronic wound healing. Ciftci *et al.* reported the preparation and characterization of PVA-chitosan composite mats by an electrospinning method for the sustained release of curcumin, which showed antioxidant and anti-microbial properties against *E. coli* and *S. aureus*.[9] Rashid *et al.* studied the role of the sustained release of curcumin from PVA-gelatin for the downregulation of pro-inflammatory cytokines for full-thickness wound healing.[10]

[a] *School of Biotechnology, University of Jammu, Jammu, J&K, 180006, India. E-mail: suhelat@gmail.com*
[b] *Department of Materials Engineering, Indian Institute of Technology Jammu, Jammu, J&K, 181221, India*
[c] *Department of Materials Science and Engineering, Indian Institute of Technology Kanpur, UP, 208016, India*
[d] *Biosciences and Bioengineering Department, Indian Institute of Technology Kanpur, UP, 208016, India*

Tamra Bhasma and *Yasad Bhasma* are two nanoformulations with origins in Rasa-Shastra of the Indian Ayurvedic medicine system. *Tamra Bhasma* (TB) has been reported to show free-radical scavenging, hepatoprotective activity and anti-inflammatory effects.[11–13] Physicochemical characterization studies and phase analysis of *Tamra Bhasma* show the presence of nano- to sub-micron-particles of copper sulfide.[14,15] *Yasad Bhasma* (YB) has also shown pharmaceutical benefits, such as antibacterial and anti-diabetic effects.[16,17] Compositional and morphological analyses of *Yasad Bhasma* have shown the presence of ZnO particles in nano- to sub-micron-ranges.[17,18] The biopharmaceutical benefits of these two Bhasmas are of significant interest with respect to diabetic wound healing. Cinnamon oil is known for its potent anti-microbial properties, which are useful in the management of infection in wounds.[19] Ahmadi *et al.* studied the antioxidant and anti-bacterial properties of *Cinnamon verum* essential oil in mice infected-wound models.[20] The study showed that topical application of cinnamon oil cream (with paraffin) to mouse wounds infected with *S. aureus* and *P. aeruginosa* bacterial strains led to a 6-fold decrease in bacterial counts on the twelfth day and granular tissue formation on the fourteenth day of treatment. However, retaining the anti-bacterial and antioxidant properties of cinnamon oil for longer durations in diabetic or chronic wounds is challenging due to loss of its chemical stability in complex micro-environments of such wound beds. Delivering cinnamon oil extract in the form of nanoemulsion particles is one strategy to ensure its sustained release in the wound bed and achieve long-term and potent antimicrobial effects. Moustafa *et al.* demonstrated the potent anti-bacterial effect of a cinnamon oil nanoemulsion delivered from a carboxymethyl cellulose–starch composite wound dressing on four bacterial strains: *S. aureus*, *B. cereus*, *Escherichia coli* and *Staphylococcus typhimurium*.[21]

In the present work, the potency of these two Ayurvedic Bhasmas, in combination with cinnamon oil nanoemulsion, was explored by loading them in a PVA-based film and sponge matrix for healing and management of infected diabetic wounds. The combined bioactive system (TB + YB + NE) was assessed *in vitro* for its antioxidant, antibacterial, pro-proliferative, pro-migratory, collagen-forming, and angiogenic effects. The results showed that these cost-effective Ayurvedic formulations have significant promise as potent healing agents for diabetic wounds, in combination with modern drug-delivery hydrogels and sponges, possessing tunable physical and mechanical properties.

1.1. Materials

Cinnamaldehyde was purchased from HiMedia (GRM3277). Polyvinyl alcohol (PVA) was procured from Loba Chemie (mol wt. 115 000, 99% hydrolysis), and glycerol was purchased from Fisher Scientific, Mumbai (India). Dulbecco's Modified Eagle's Medium (Thermo Fisher, 12100046), high glucose media, and trypsin-ethylenediaminetetraacetic acid (Trypsin-EDTA Thermo 25200072) were purchased from Thermo Fisher Scientific, Mumbai (India). Medium chain triglyceride oil (MCT) was procured from Novus Life Science, Mumbai, India (caprylic : capric acid = 60 : 40), and fetal bovine serum (FBS), of EU-approved South American origin, was procured from Gibco, Mumbai (India). NIH 3T3 cells were obtained from the National Centre for Cell Science (NCCS), Pune (India). HaCaT cells were kindly provided by Prof Kaushik Chatterjee (IISc Bangalore). HUVEC cells were kindly provided by Prof Ashok Kumar (IIT Kanpur). Alamar Blue was purchased from Himedia (India). *Pseudomonas aeruginosa* (MTCC-3541) and *Staphylococcus aureus* (MTCC-96) were procured from MTCC, Chandigarh (India). Pecam-1 (Abcam ab28364). *Tamra* and *Yasad Bhasma* were procured from a local market in India.

2. Methods

2.1. Preparation of cinnamon oil NE

Cinnamaldehyde and medium-chain triglyceride were mixed in a ratio of 1 : 10. Tween 80 (3 mL) was added to the prepared CBO-MCT (cannabichromene + medium-chain triglyceride) mixture (5 mL) and stirred for 30 min at 800 rpm. To this, DI water (42 mL) was added dropwise using a 200-microliter pipette to obtain a coarse emulsion. This emulsion was further subjected to ultrasonication at 40% amplitude for 15 min under ice with a 9-s on–off cycle to obtain a nanoemulsion. The as-prepared nanoemulsion was used for further characterizations and *in vitro* studies.

2.2. Characterization of Bhasmas and cinnamaldehyde nanoemulsion

The procured Bhasmas and synthesized nanoemulsion were subjected to morphological and physicochemical analysis. The size distribution of the Bhasma and nanoemulsion was obtained by dynamic light scattering (DLS). The hydrodynamic size distribution of the synthesized samples was determined using a Litesizer 500 (Anton Paar, Austria) instrument. Measurements were performed at a temperature of 25 °C ± 0.1 °C using quartz cuvettes in deionized water as the dispersing medium. The solvent refractive index and viscosity were set at 1.3303 and 0.8903 mPa s, respectively. Each sample was equilibrated for 2 min prior to analysis, and measurements were taken in automatic scattering mode with multiple short runs (10 s each) processed using the general cumulant analysis model. The morphological and microstructural analysis of the synthesized samples was carried out using transmission electron microscopy (TEM). A small quantity of the dried sample was ultrasonically dispersed in ethanol (99.9%) for 10 minutes to ensure uniform dispersion. A drop of the well-dispersed suspension was then placed onto a carbon-coated copper grid and air-dried at room temperature before imaging. The samples were observed under a high-resolution transmission electron microscope (JEOL JEM-2100) to capture images at various magnifications. The micrographs obtained were analyzed to determine particle morphology. Nanoemulsion particle morphology was also visualized under a Jeol high-resolution transmission electron microscope operating in the bright-field mode. The crystalline structure and phase composition of the synthesized samples were analyzed using X-ray diffraction

(XRD). XRD patterns were recorded on an X-ray diffractometer (PANalytical X'Pert PRO/Bruker D8 Advance) equipped with a Cu Kα radiation source (λ = 1.5406 Å), operated at 40 kV and 30 mA. The phase composition of as-received *Tamra Bhasma* and *Yasad Bhasma* samples was studied with a PANalytical X'pert diffractometer with Bragg–Brentano geometry. The wavelength used was Cu-Kα with a line detector. The scan angle was taken between 20°–100° at a scan rate of 1° min^{-1}. The peaks were indexed by reference to the standard Pearson's crystallographic database.

2.3. Optimization of the Bhasma and NE concentrations

The biocompatibility of *Tamra Bhasma*, *Yasad Bhasma* and nanoemulsion was evaluated on NIH 3T3 fibroblast cells using the Bhasma- and nanoemulsion-spiked media. The spiked media was prepared by adding different concentrations of Bhasma and nanoemulsion in serum-free media. The spiked media was filter-sterilized (0.22 micron) and added with FBS (10%) and antibiotic (1%) to make complete media. The fibroblast cells were cultured in DMEM media, 10% FBS and 1% penicillin/streptomycin at 37 °C with 5% CO_2. Around 1×10^4 cells were seeded per well and incubated for 24 h to allow attachment; thereafter, the media was replaced with complete spiked media and incubated for 48 h at 37 °C. Cells without any bioactives served as a 2D positive control. The cell viability was evaluated by Alamar Blue assay and live/dead staining.

2.3.1. Alamar blue assay. Following incubation, the media was replaced with Alamar Blue solution (33 μM) and incubated for 4 h. The supernatant was assayed at 530/590 nm using a plate reader (Biotek Gen5). The results were reported as a percentage of the positive control.

2.3.2. Live dead staining. The cells following incubation were washed with warm PBS and incubated for 30 min with calcein AM and propidium iodide as per the manufacturer's instructions, and imaged using a fluorescent microscope (Leica DMi8).

2.4. Preparation of the PVA film and sponge loaded with *Tamra Bhasma*, *Yasad Bhasma* and nanoemulsion

For the preparation of the bioactive-loaded PVA hydrogel film, the required amounts of *Tamra* and *Yasad Bhasma* were suspended in 10 mL of DI water and subjected to probe sonication at 40% power for 10 min. Separately, PVA was dissolved in 40 mL DI water at 90 °C to prepare a 7.5 wt% PVA solution. After complete dissolution of PVA, the solution was cooled to room temperature, and the required amounts of Bhasma solution and cinnamaldehyde nanoemulsion were added dropwise under stirring for another 30 min. The cooled solution was cast in a 90 mm Petri dish and dried at room temperature to prepare the bioactives-loaded PVA hydrogel films.

To prepare the sponge, bioactive-loaded solution (PVA 5% w/v) was prepared as described for the PVA film, and the cooled solution was poured into a 2 mL syringe and frozen at −80 °C overnight, followed by lyophilization (Labconco 2.5 L) to obtain the cryogel sponges.

PVA films and sponges without any additives (TB, YB, and NE) were prepared as controls. The films and sponges with all additives were named PVA TYN Films and PVA TYN Sponges, respectively.

2.5. Material testing and characterization studies

The morphological features of the synthesized PVA TYN films and PVA TYN sponges were examined using scanning electron microscopy (SEM). The PVA TYN sponges were cut into cross-sectional discs (2 mm thickness, 5 mm diameter) to observe the internal porous architecture. The samples were sputter-coated with gold for 180 seconds using a sputter coater (EMLTECH 7620) and observed under SEM (Carl Zeiss EVO 50). The pore size was analyzed from SEM micrographs using the ImageJ software. For each formulation, three independent sponge samples were analyzed, and 3–4 representative images were captured per sample. The porosity of the cryogels was further quantified using the liquid displacement method with cyclohexane as a non-wetting solvent.[22] Circular discs of 5 mm × 5 mm were weighed (W_1), submerged in cyclohexane to measure the immersed weight (W_2), and then reweighed after removal (W_3). Porosity (%) was calculated using the following relation:

$$\text{Porosity}\,(\%) = \frac{W_1 - W_3}{W_2 - W_3} \times 100. \quad (1)$$

The mechanical properties of the PVA TYN films were evaluated using an Instron Universal Testing Machine (Model 3345). The thickness of each sample was measured using a micrometer (Mitutoyo Corporation, Japan) prior to testing. The tensile strength and elongation at break of the hydrogel films were determined in accordance with ASTM D882-12 standards. Film specimens of dimensions 70 mm × 10 mm (length × width) and thickness 200 ± 10 μm were cut with a gauge length of 40 mm. Prior to testing, the samples were immersed in phosphate-buffered saline (PBS, pH 7.4) for 24 hours at 37 °C to attain equilibrium swelling, ensuring evaluation under physiologically relevant hydrated conditions. The tensile test was performed at a crosshead speed of 10 mm min^{-1}, and tensile strength (MPa) and elongation at break (%) were obtained from the stress–strain curves. For compressive testing, PVA TYN sponges were cut into cylindrical discs (5 mm diameter × 8 mm height) and similarly pre-soaked in PBS for 24 hours before measurement, as per a previously published protocol.[22] The hydrated samples were tested using a Universal Testing Machine (BiSS India) equipped with a 100 N load cell. Compression was applied at a rate of 6 mm min^{-1} until the samples were 70% compressed. The compressive strength and compressive modulus were calculated from the resulting stress–strain data. The swelling behavior of the additive-loaded PVA TYN films and sponges was evaluated in phosphate-buffered saline (PBS, pH 7.4) at 37 °C under static conditions to simulate physiological environments. Pre-weighed dry samples (W_0) were immersed in PBS and withdrawn at predetermined time intervals. For PVA films, swelling was monitored at 30 min and 1, 2, 4, 8, 12, 24 h. For PVA TYN sponges, swelling was measured at

30 s, 1 m, 2 m, 5 m, 10 m, 30 m, 1 h, 2 h, 4 h, 12 h and 24 h. At each interval, samples were carefully removed, blotted with filter paper and weighed (W_t). The swelling (%) was calculated using the following relation:

$$\text{Swelling}\,(\%) = \frac{W_t - W_0}{W_0} \times 100. \quad (2)$$

The water–vapor transmission rate (WVTR) of the PVA-based films was determined using the ASTM E96-96 (inverted cup method) with slight modifications. A 25 mL glass bottle was filled with reverse osmosis (RO) water, leaving approximately $\frac{1}{2}$ inch headspace. Circular film specimens (18 mm diameter) were mounted over the mouth of the bottle and sealed with vacuum grease and paraffin wax to ensure airtight attachment. The open bottle served as a positive control, while a rubber-sheet-sealed bottle was used as a negative control. The initial weight (W_0) was recorded at t = 0, and subsequent weights were measured every 24 hours for seven days. The WVTR (g cm^{-2} day^{-1}) was calculated using the following formula:

$$\text{WVTR} = G/tA \quad (3)$$

where G/t is the slope obtained from the linear plot of weight loss (g) *versus* time (h), and A represents the film's exposed area (cm^2).

2.6. Release kinetics study of TB, YB and NE from PVA TYN film and sponge

The release kinetics of TB, YB and NE were obtained by incubating 1 × 1 cm^2 PVA hydrogel films and sponge disks (5 mm diameter × 2 mm height) in DI water for varying time intervals. Following incubation, the supernatants of the Bhasma-loaded samples were collected and digested in nitric acid. The concentration of released TB and YB in water was evaluated by ICPMS measurements after serial dilution. The concentration of these Bhasmas with time was plotted as a release rate kinetics graph. The release kinetics of NE were studied by UV-vis spectroscopy.[23] The supernatant of the samples was collected as mentioned above for the Bhasma samples. The concentration of cinnamaldehyde was calculated from the standard graph. The release kinetics graph was further plotted as percentage release kinetics.

2.7. Biological evaluation of additive-loaded PVATYN films and sponges

2.7.1. DPPH antioxidant assay. The antioxidant activity of the prepared PVA TYN films and sponges was evaluated using the 2,2-diphenyl-1-picrylhydrazyl (DPPH) radical scavenging assay. Pre-cut samples of standard dimensions (1 × 1 cm^2) were immersed in 1 mL of 100 μM methanolic DPPH solution and incubated at 37 °C for 45 minutes in the dark to prevent photodegradation. The absorbance (OD) of the DPPH solution was recorded at 517 nm using a UV-vis spectrophotometer (Thermo, Evolution 201) both before incubation (A_0) and after incubation with each sample (A_t). The OD of DPPH alone after incubation was subtracted from all the values to normalize the self-dissociation of DPPH. The antioxidant activity is calculated as follows:

$$\text{Antioxidant activity}\,(\%) = \frac{A_0 - A_t}{A_0} \times 100, \quad (4)$$

where A_0 is the absorbance of the DPPH solution without the sample, and A_t is the absorbance after incubation with the film or sponge. A higher percentage reduction in absorbance showed greater antioxidant potential due to more effective free-radical scavenging.

2.7.2. Haemocompatibility assay. The hemocompatibility of the bioactive-loaded PVA TYN films and sponges was evaluated according to ASTM F756-17 using a goat red blood cell (RBC) suspension, as per previously published literature.[24] The RBC suspension was prepared as per the standard procedure. Freshly collected goat blood (5 mM EDTA) was centrifuged at 5000 rpm for 10 minutes, the supernatant was discarded, and the RBC pellet was washed repeatedly with phosphate-buffered saline (PBS, pH 7.4) until a clear supernatant was obtained. The final RBC suspension was stored at 4 °C until use. Film samples (1 × 1 cm^2) and sponge discs (5 mm × 2 mm) were equilibrated in 200 μL PBS for 10 minutes, followed by the addition of 800 μL of the RBC suspension to minimize osmotic shock. Samples were then incubated at 37 °C for 90 minutes in a dry bath. The positive control was prepared by adding 2 μL of Triton X-100 to induce complete haemolysis, while untreated RBCs in PBS served as the negative control. Following incubation, samples were centrifuged at 5000 rpm, and the absorbance of the supernatant was recorded at 540 nm. The percentage haemolysis was calculated using the following formula:

$$\%\text{Haemolysis} = \frac{A_{\text{sample}}}{A_{\text{positive control}}} \times 100, \quad (5)$$

where A denotes the absorbance at 540 nm.

2.7.3. Antimicrobial tests. The antimicrobial potential of the prepared sample was evaluated by zone of inhibition and time kill assays on one Gram-positive (*Staphylococcus aureus* MTCC 96) and one Gram-negative species (*Pseudomonas aeruginosa* MTCC 3541). The two bacterial species, *S. aureus* and *P. aeruginosa*, were revived from their stock on nutrient agar plates, and a single colony of the respective species was cultured overnight in Muller–Hinton (MH) broth. The overnight cultures were used to perform zone of inhibition and time kill assays. Zone of Inhibition assays were performed as per the modified CLSI standard (M02). The fresh overnight culture of bacteria was spread on the Muller–Hinton agar plate with 10^5 CFU. All the film samples (1 × 1 cm^2) were dipped in 1 mL PBS for 24 h at 37 °C to release the bioactives. Whatman filter paper was punched to obtain a disc of diameter 5 mm and left under UV overnight to sterilize the surface. These discs were dipped in the overnight leach-out solution and inserted on bacterial plates and incubated for 24 h at 37 °C. Filter paper discs dipped in povidone iodine and PBS served as positive and negative controls, respectively. Time kill assays were performed in Muller–Hinton Broth as per the modified CLSI standard (M07). The samples (1 × 1 cm^2) were surface sterilized by

overnight under UV and incubated with bacterial culture 10^5 CFU mL^{-1} at 37 °C for 24 h. Following incubation, the killing of bacterial cells was evaluated using the resazurin assay. Briefly, 30 μL of 0.15% resazurin solution was added to the bacterial suspension and then incubated for 2 h in a 48-well plate. Then, the fluorescence of the solution was obtained at 535 nm and 590 nm for emission and excitation wavelengths, respectively. Iodine incubated solutions were taken as the positive control, and the bacterial solution without treatment was taken as the negative control. The percentage of bacteria killed was obtained by the following equation:

$$\%\text{Killing} = \frac{\text{Fluorescence of positive control} - \text{Fluorescence of sample}}{\text{Fluorescence of positive control} - \text{Fluorescence of negative control}} \times 100 \quad (6)$$

2.7.4. Biofunctional assays. The biofunctional potential of TB and YB incorporated within the PVA TYN films and sponges was evaluated through key wound-healing parameters, including cell proliferation, migration, collagen synthesis, angiogenesis, and free-radical scavenging. Experiments were performed using fibroblasts (NIH 3T3), keratinocytes (HaCaT), and endothelial cells (HUVEC) to represent the major cell types involved in cutaneous repair.

2.7.5. Preparation of conditioned media. Square samples of PVA TYN films and sponges were incubated in Dulbecco's Modified Eagle Medium (DMEM) without fetal bovine serum (FBS) at 37 °C for 24 hours to simulate the physiological release of bioactive components. The sample-to-medium ratio was maintained at 1 cm^2 mL^{-1}, corresponding to the typical exudate turnover rate in moderately to highly exudating wounds (0.5–1 mL cm^{-2} day^{-1}).[25] After incubation, the samples were removed, and the collected extract was supplemented with 10% FBS and 1% antibiotic–antimycotic solution to prepare complete conditioned media. For endothelial cell experiments, Endothelial Cell Growth Medium (Merck 211-500) was used instead of DMEM. The resulting conditioned media were used for all subsequent biofunctional assays.

2.7.6. Cell proliferation assay. The effect of the released Bhasma and NE components on cell proliferation was assessed using the Alamar Blue metabolic assay, Ki-67 immunostaining, and live/dead staining. Fibroblast (7500 cells per well) and keratinocyte (10 000 cells per well) cells were seeded in 48-well plates and allowed to attach for 24 hours. The medium was then replaced with the prepared conditioned media, and cells were incubated for 1, 3, and 5 days, with media renewal every 48 hours. Endothelial cells (HUVECs) were cultured in endothelial expansion media and seeded at a density of 5000 cells per well under the same treatment. Cell proliferation was quantified by measuring metabolic activity *via* Alamar Blue reduction (fluorescence at 560/590 nm). In parallel, Ki-67 staining was used to visualize actively proliferating nuclei, and phalloidin/DAPI co-staining was performed to examine cytoskeletal organization and nuclear integrity. Live/dead assays further confirmed the overall cell viability and biocompatibility.

2.7.7. Collagen production assay. The influence of the release of TB, YB and NE on collagen synthesis was determined using Picrosirius Red staining. Fibroblast (NIH 3T3) and keratinocyte (HaCaT) cells were seeded as described in the proliferation assay. After treatment with conditioned media for 3 days, cells were fixed using Kahale's fixative and stained with 1% Sirius Red solution for 30 minutes. Excess dye was removed by gentle washing, and the bound stain was eluted in 0.1 N NaOH. Absorbance was measured at 540 nm, and collagen content was expressed as a fold change relative to untreated control cells. This assay quantified the ability of the released TB and YB to stimulate ECM protein (collagen) synthesis, an essential step in wound remodelling.

2.7.8. Cell migration (scratch) assay. The effect of Bhasma release on cell migration was evaluated using wound scratch assays on fibroblast (NIH 3T3) and keratinocyte (HaCaT) monolayers. Cells (50 000/well) were seeded in DMEM containing 10% FBS and cultured for 16 hours to form a uniform confluent layer. The medium was replaced with 1% FBS DMEM containing Mitomycin C (5 μg mL^{-1}) for 3 hours to inhibit proliferation. A uniform scratch was made using a sterile 200 μL pipette tip, and the detached cells were gently washed away with warm PBS. The cells were then treated with conditioned media containing 5% FBS and incubated at 37 °C. Scratch closure was monitored under an inverted microscope at 0 h and 24 h, and subsequent intervals until closure was complete. Migration efficiency was quantified as the percentage of wound closure using the ImageJ software.

2.7.9. Angiogenesis assay. The angiogenic potential of the released bioactives was investigated using CD31 immunofluorescence staining in HUVEC cells. Endothelial cells were cultured with conditioned media for 1, 3 and 5 days. Following incubation, cells were fixed with 4% paraformaldehyde, permeabilized, and stained with anti-CD31 antibody, followed by a fluorescent secondary antibody.

2.7.10. Free radical scavenging. The cellular ROS scavenging ability of nanobhasmas released was evaluated using menadione-induced oxidative stress in fibroblasts. NIH 3T3 cells (10 000 cells per well) were seeded in a 48-well plate and allowed to attach for 24 hours. The cells were pre-treated with conditioned media for 12 hours, followed by exposure to menadione (5.8 mM) for 2 hours to induce ROS production. After washing with PBS, the cells were incubated with 2 μM DCFH-DA for 30 minutes to detect intracellular ROS levels. Lower fluorescence intensity showed enhanced antioxidant protection mediated by the released Bhasma and NE components.

2.7.11. Statistical analysis. One-way ANOVA was performed to determine statistical significance between appropriate groups. Description of the groups between which ANOVA was calculated is mentioned in the caption of each figure. A p-value ≤ 0.05 was considered significant. In the figures, a single "*" corresponds to a p-value ≤ 0.05, a double "**" star corresponds

to a *p*-value ≤ 0.01, a triple star "***" corresponds to a *p*-value ≤ 0.001, and a quadruple star "****" corresponds to a *p*-value $\leq$ 0.0001.

3. Results and discussions

3.1. Characterization of Bhasmas and synthesized cinnamon bark oil nanoemulsions

The particle size distributions of as-received *Tamra Bhasma* and *Yasad Bhasma* and the as-prepared nanoemulsion are shown in Fig. 1(a–c). The average particle sizes for *Tamra Bhasma*, *Yasad Bhasma* and NE were found to be 255 nm, 270 nm and 190 nm, respectively. The TEM micrographs (Fig. 1(d–f)) revealed distinct morphological differences among the three samples. The nanoemulsion showed a uniform, spherical morphology with a size distribution of 150–250 nm and an average size of 190 nm. The particles appeared well-dispersed with minimal aggregation, indicating efficient emulsification and good colloidal stability. The smooth contrast and absence of sharp crystalline boundaries suggest that the droplets were amorphous or liquid-like in nature (Fig. 1(a and d)). The Tamra sample displayed aggregated clusters of near-spherical nanoparticles, with individual particle sizes primarily in the range of 170–300 nm, with an average particle size of 250 nm (Fig. 1(b and e)). The TEM image showed irregularly shaped particle morphology with varying sizes, which might be due to particle aggregation (Fig. 1(e)). The Yasad sample exhibited a size distribution similar to that of *Tamra Bhasma* particles, with an average size of around 270 nm (Fig. 1(c and f)). Fig. 1(f) shows the TEM micrograph of *Yasad Bhasma*, which exhibits particles of various sizes arising from aggregation. The phase composition of the two Bhasmas was analyzed by X-ray diffraction. Fig. 1(g and h) shows the X-ray diffractogram of Tamra and Yasad Bhasma with CuS

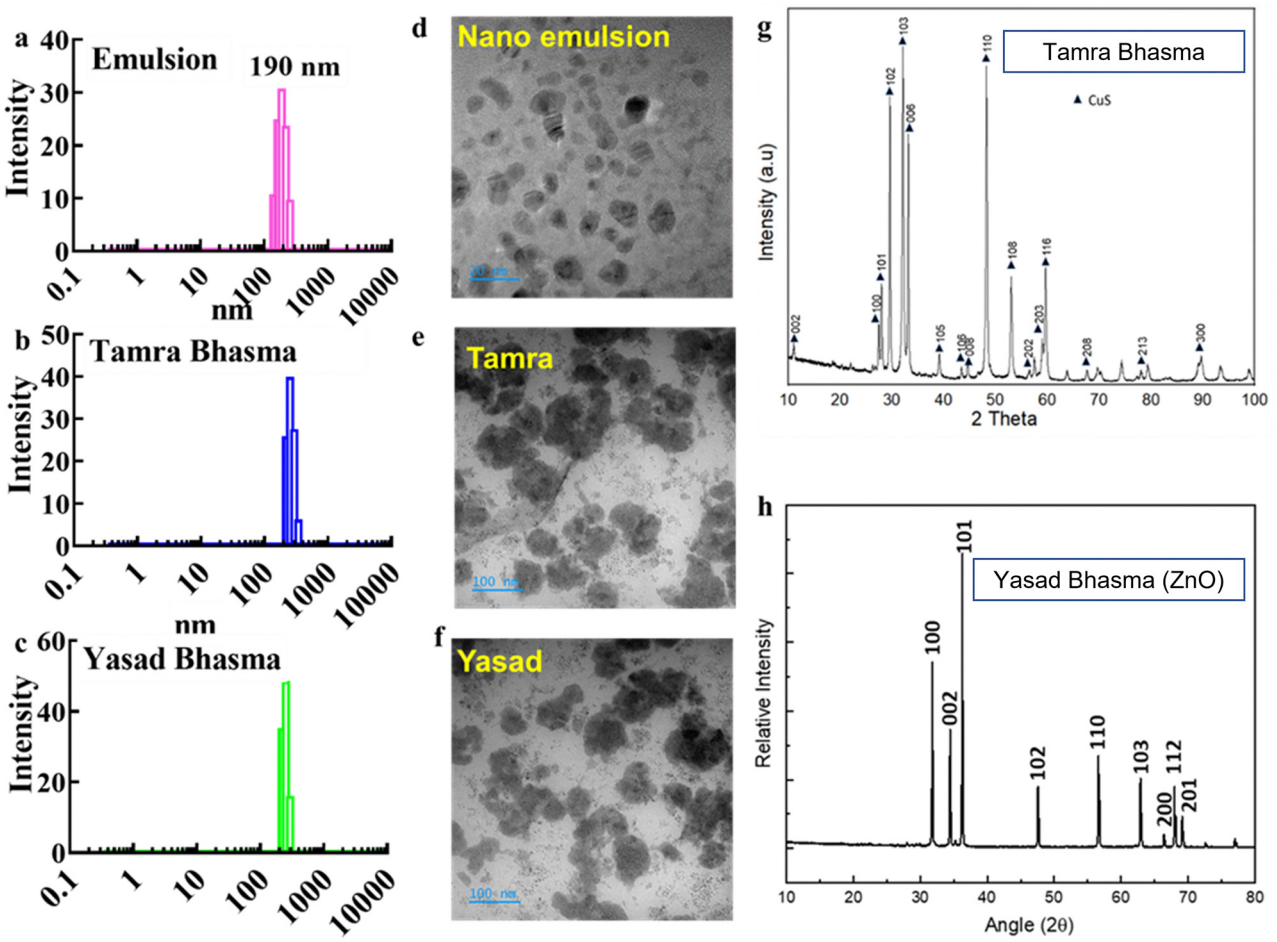

Fig. 1 Physicochemical characterization of *Tamra Bhasma* (CuS), *Yasad Bhasma* (ZnO), and cinnamaldehyde NE. Dynamic light scattering (DLS) analyses revealed narrow particle size distributions for (a) NE (b) TB and (c) YB, showing stable dispersions with mean hydrodynamic diameters within the nanoscale range and low polydispersity indices. Transmission electron microscopy (TEM) micrographs showing (d) spherical to irregular nanoemulsion particles with uniform dispersion and no visible aggregation; (e) *Tamra Bhasma*, with distinct nanosized clusters corresponding to copper sulfide (CuS), and (f) *Yasad Bhasma*, with crystalline ZnO particles of comparable dimensions. X-ray diffraction (XRD) patterns confirmed the crystalline phases of *Tamra Bhasma* (CuS) (g) and *Yasad Bhasma* (ZnO) (h). Characteristic peaks at 2θ = 27.6°, 29.3°, 47.9°, and 54.8° correspond to the CuS planes (JCPDS 06-0464), while peaks at 31.7°, 34.4°, 36.2°, 47.5°, and 56.6° match the ZnO reflections (JCPDS 36-1451). The sharp diffraction peaks show high crystallinity and phase purity of both Bhasmas. Scale bars = 100 nm.

and ZnO being the major detectable phases, respectively. The sharpness of the peaks indicates high crystallinity, and the absence of additional impurity peaks suggests successful phase formation during the calcination process in Bhasma preparation.

3.2. Optimization of the Bhasma and NE concentrations

The useful concentrations of Bhasma and NE that could be loaded on the PVA matrix for the fabrication of the film and sponge dressing were determined by viability assays with fibroblast cells. The concentrations of Bhasma from 500 μg mL^{-1} to 6.25 μg mL^{-1} were evaluated by preparing Bhasma-containing DMEM media with concentrations of 500, 250, 125, 75, 37.5, 18.75 and 9.5 μg mL^{-1}. Similarly, nanoemulsions with concentrations of 50, 25, 12.5, 6.25, 3.12 and 0.75 μL mL^{-1} were evaluated. The minimum concentration that resulted in a viability of more than 80% after 48 h was selected to fabricate the dressing material. The results are presented in Fig. 2(a and b).

3.3. Preparation and characterization of Bhasma- and NE-loaded PVA hydrogel films and PVA cryogel sponges

The macroscopic appearance of the fabricated PVA TYN hydrogel films and sponges revealed structural uniformity. The films exhibited smooth surfaces while the lyophilized sponges retained their shape integrity and exhibited a porous, foam-like structure (Fig. 3(a)). The SEM micrograph of the sponge (Fig. 3(b)) shows an interconnected porous architecture with pore sizes in the range of 50–150 μm. The EDS mapping (Fig. 3(b)) confirmed the homogeneous distribution of Cu, Zn, S, C, and O, indicating uniform incorporation of TB (CuS) and YB (ZnO) within the PVA matrix. The porosity measurements shown in Fig. 3(d and e) indicated a high interconnected void fraction (85%), facilitating high exudate retention and nutrient exchange. The contact angle measurement (Fig. 3(c)) demonstrated enhanced hydrophilicity of the PVATYN films compared to native PVA. The improved wettability can be attributed to the incorporation of polar metal oxide species (CuS, ZnO) and NE, increasing surface energy and water affinity. The increased hydrophilicity ensures nonadherence of the dressings, resulting in painless dressing changes and negligible damage to regenerating tissue.[26] The tensile and compressive properties of the PVA TYN composites (Fig. 3(h and i)) revealed a significant enhancement compared to native PVA films and sponges. The tensile strength of the swelled PVATYN film increased to 1.6 MPa, with an elongation at break of 200%, compared to 0.5 MPa and 80%, respectively, for pure PVA. Similarly, the compressive strength of the swelled sponge improved from 0.35 MPa (control) to 0.5 MPa, and the compressive modulus increased from 1.0 to 1.3 MPa, respectively. These improvements can be attributed to the reinforcing effects of metallic nanoparticles and the plasticizing effect of the nanoemulsion between PVA hydroxyl groups. The swelling kinetics of the PVATYN films and sponges (Fig. 3(f and g)) demonstrated a rapid initial uptake within the first few hours, followed by a gradual equilibrium phase. The equilibrium swelling ratio of cryogels reached 400%, significantly higher than that of the films (180%), owing to their open-pore network and higher water-retention capacity. The slight reduction in swelling compared to pure PVA can be attributed to enhanced

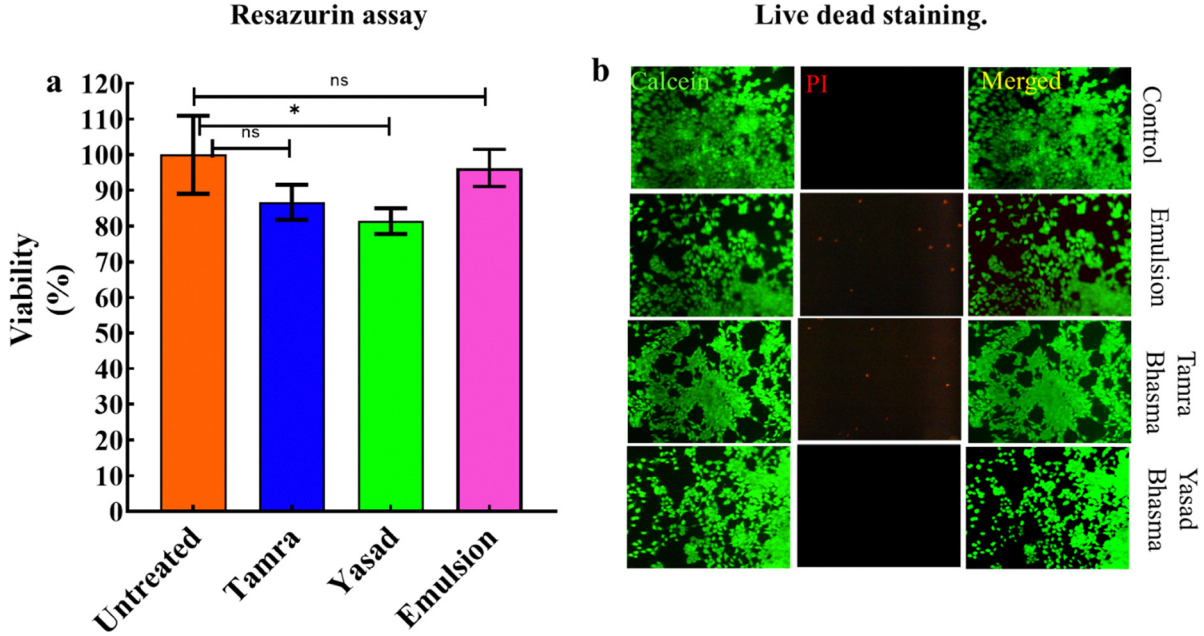

Fig. 2 Optimization of *Tamra Bhasma*, *Yasad Bhasma*, and NE concentrations for fibroblast viability. Cell viability of NIH 3T3 fibroblasts after 48-h exposure to varying concentrations of bioactives. TB (250 μg mL^{-1}), YB (25 μg mL^{-1}), and NE (3.12 μL mL^{-1}), as determined by an Alamar Blue assay (a). Values represent mean ± SD (n = 3). (b) Live/dead fluorescence staining of the fibroblast cells cultured with optimized concentrations of bioactives for 48 h, showing predominantly viable cells (Calcein-AM, green) and negligible dead cells (Propidium iodide, red). The fluorescence images confirm the high cytocompatibility of all three bioactives at the selected concentrations, confirming their suitability for incorporation into PVATYN films and sponges. Scale bar = 100 μm.

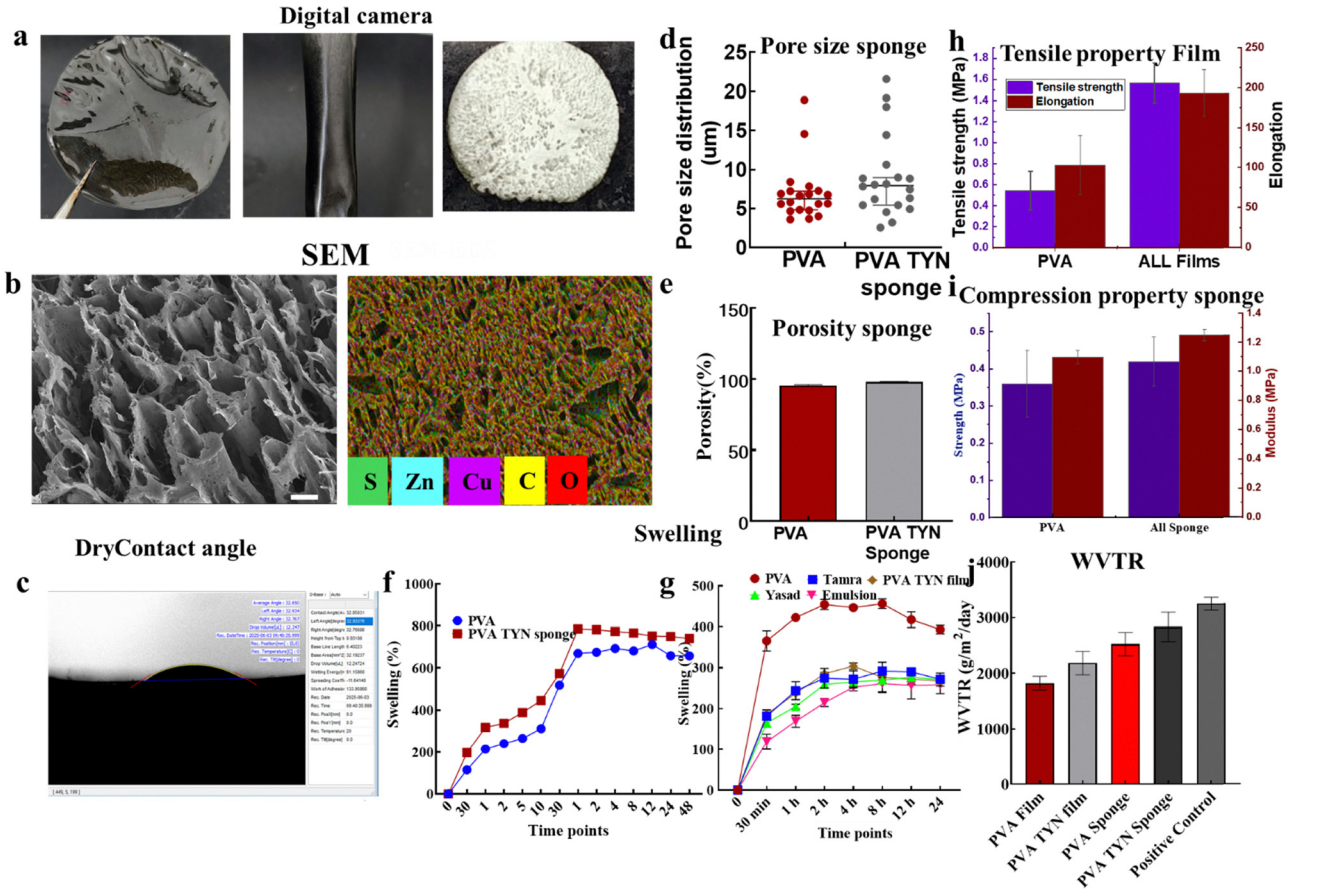

Fig. 3 Physicochemical and mechanical characterization of the PVA TYN films and cryogel sponges. Macroscopic appearance of the PVATYN hydrogel film and lyophilized sponge showing the uniform structure and flexibility (a). Representative SEM image of the porous architecture of the PVATYN sponges along with EDS elemental mapping confirming the uniform presence of sulfur (S), zinc (Zn), copper (Cu), carbon (C), and oxygen (O) derived from YB, TB and the PVA matrix (b). Contact angle (dry state) (c). Pore size distribution plot showing the interconnected porous structure conducive to nutrient exchange and cell infiltration (d) and (e). Swelling kinetics of the PVATYN films (f) and sponges (g) in PBS (pH 7.4 and 37 °C), demonstrating rapid initial uptake followed by equilibrium hydration; sponges exhibit higher swelling capacity due to their open porous structure. Mechanical properties of the PVATYN films indicate enhanced strength and modulus compared with PVA; the composite demonstrates improved elongation and mechanical resilience suitable for wound dressing applications (h) and (i). Water–vapor transmission rate (WVTR) showing that the incorporation of bioactive additives slightly reduced vapor transmission while maintaining the optimal moisture balance for wound healing (j).

crosslink density resulting from interactions of the Bhasma ions and the NE with the PVA chains. The water–vapor transmission rate (WVTR) (Fig. 3(j)) of the PVA–TYN films was found to be within the optimal range of 2000–2500 g m^{-2} day^{-1}, making it suitable for wound-healing applications that require balanced moisture permeability. The marginal decrease in the WVTR of PVA–TYN films compared with that of pristine PVA reflects the improved barrier properties with the incorporation of Bhasma particles.

3.4. DPPH, antimicrobial and hemolysis assays

The free-radical scavenging properties of the PVA film and sponge loaded with Bhasma nanoemulsion and bioactive agents were studied with DPPH assays, as shown in Fig. 4(a). Around 80% of free-radical scavenging was observed for the YB, NE and PVA TYN films and sponges, while the TB and PVA films showed less than 50% free radical scavenging. The antimicrobial properties of the individual Bhasmas, NE and PVA films were evaluated by time kill assays performed with *S. aureus* and *P. aeruginosa* bacterial species (Fig. 4(b and d)). Iodine-incubated bacterial solutions were taken as the positive control, while untreated bacteria were taken as the negative control. All the sample groups, except for the PVA film and sponge, showed killing above 80% for *S. aureus* and *P. aeruginosa*. Hemocompatibility of the sample groups was tested on goat's blood. All the sample groups showed less than 5% hemolysis, establishing their hemocompatibility with respect to the known hemolytic material Triton-X (Fig. 4(c)).

3.5. Release kinetics

The efficacy of the loaded bioactive agents, TB, YB and NE, is dependent on their release kinetics and release percentage. Release kinetics and cumulative release of the Bhasma ions (Cu and Zn) and NE were found to be faster in the sponge than in the PVA film. The Bhasma ions (Cu and Zn) showed a cumulative release of around 50% for Cu and 60% for Zn loaded in

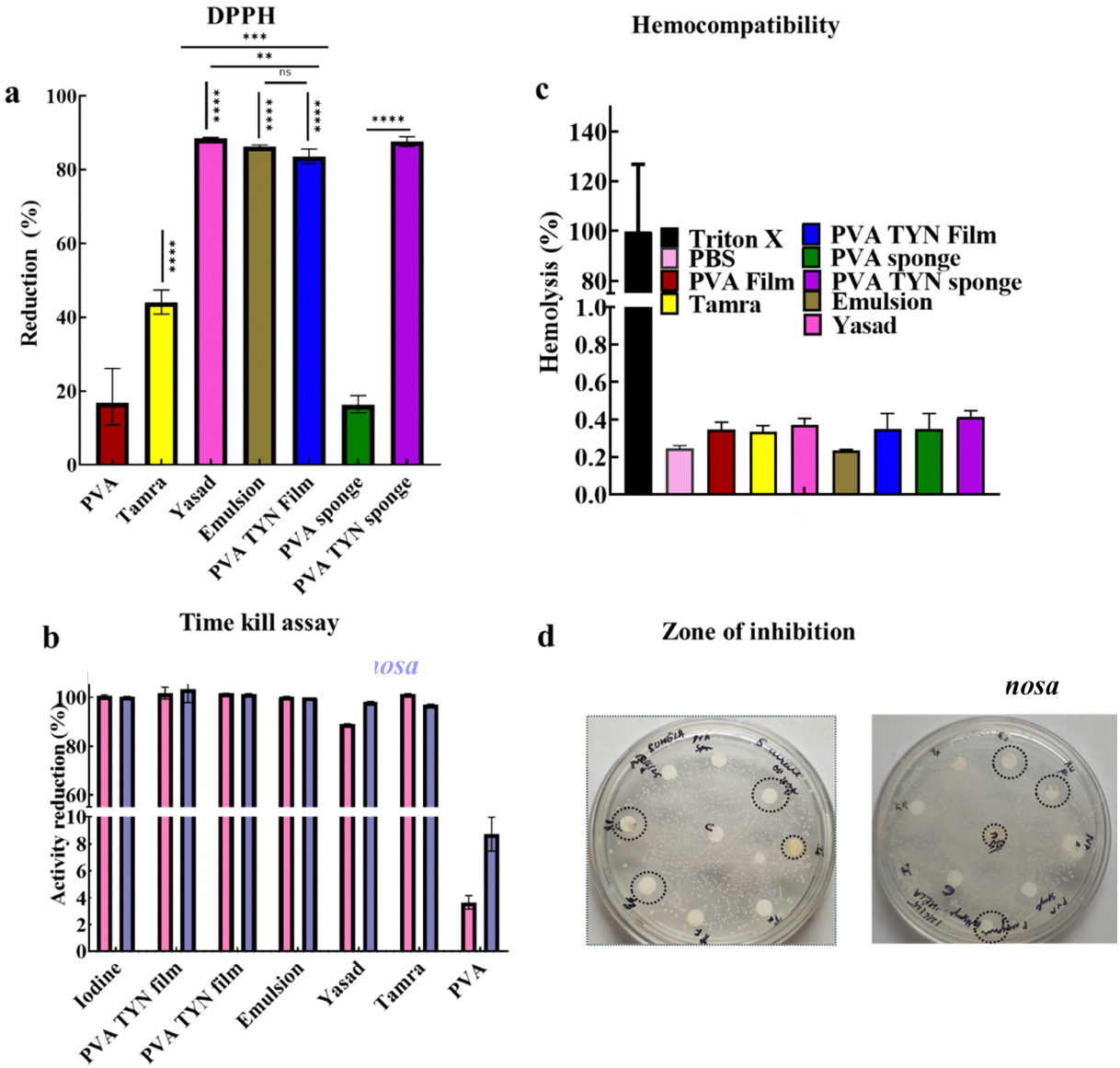

Fig. 4 Evaluation of the antioxidant, hemocompatible, and antimicrobial performance of the PVATYN films and sponges. DPPH free-radical scavenging assays showing percentage reduction in DPPH absorbance at 517 nm for different PVATYN formulations, indicating enhanced antioxidant potential upon the incorporation of TB, YB, and NE (a). Hemocompatibility analysis based on the percentage hemolysis of goat red blood cells (RBCs) exposed to PVA–TYN samples, confirming <5% hemolysis across all formulations, within ISO 10993–5 acceptance limits for non-hemolytic biomaterials (b). Time-kill rate of PVA–TYN films and sponges against *Staphylococcus aureus* (Gram-positive) and *Pseudomonas aeruginosa* (Gram-negative), showing significant reduction in bacterial viability after 24-h incubation compared with control (c). Zone of inhibition assay illustrating the antibacterial activity of PVA–TYN films and sponges against *S. aureus* and *P. aeruginosa* (d). PBS- and povidone–iodine-treated discs served as negative and positive controls, respectively. The presence of distinct inhibition zones confirms the synergistic antimicrobial effects of CuS (*Tamra Bhasma*), ZnO (*Yasad Bhasma*), and cinnamon oil NE in the composite matrix.

film, while for the sponge, the cumulative release was around 65% for Zn and 70% for Cu ions (Fig. 5(a)). The cumulative release percentages of NE were found to be higher than those of the Bhasma ions, with around 70% cumulative release for the film and 80% for the sponge (Fig. 5(b)). The release for all the bioactive formulations reached saturation after 24 h of incubation with DI water. To obtain the release behavior of the formulations, kinetic models were fitted to cumulative releases of Bhasma ions and NE. As per the reported literature, two widely used models for the release of nanoparticles/drugs from hydrogel and sponge matrix are the Higuchi and Korsmeyer–Peppas models.[27–29] The nanoparticles and cinnamon NE release were modeled as per the two models. Based on the R-square values, all the bioactive agents, Zn ions, Cu ions, and cinnamon oil NE, were observed to follow the KP model, with an n value less than 0.45, suggesting the Fickian diffusion-controlled release of these formulations from the PVA film and sponge.

The release of cinnamaldehyde nanoemulsion (NE) from the PVA matrix is primarily governed by diffusion-driven transport,

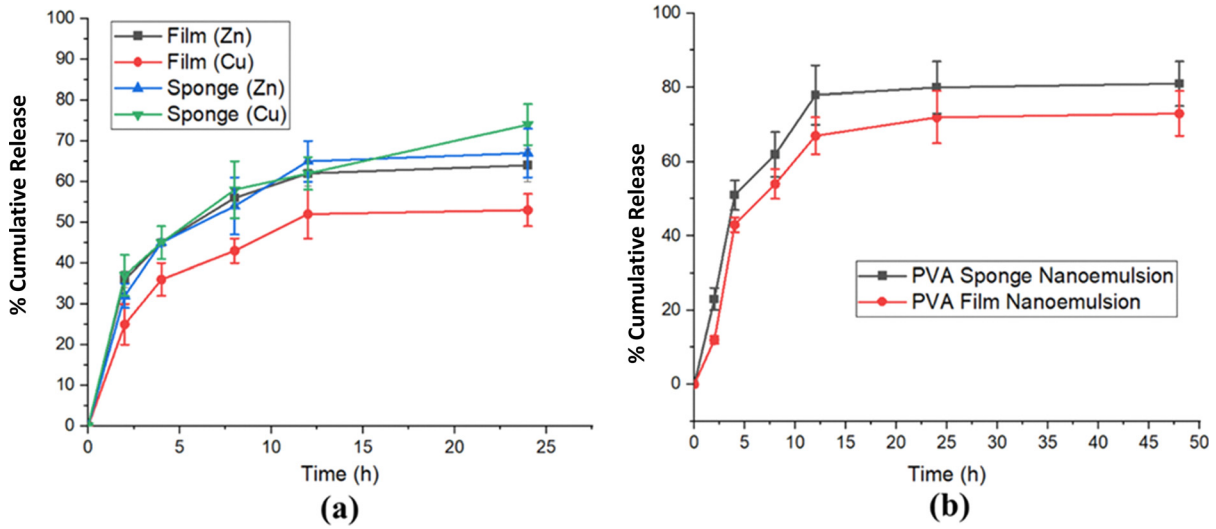

Fig. 5 Percentage cumulative release kinetics of (a) *Tamra* and *Yasad Bhasma* loaded in the PVA film and sponge and (b) NE loaded in the PVA film and sponge.

Table 1 Summary of the model-fitted parameters for the Higuchi and KP models of the release profile of zinc ions, copper ions (obtained from ICPMS) and the nanoemulsion loaded in the PVA film and sponge

Sample release	Higuchi model (K_H and R^2 values)	KP model (K and R^2 values)
Zn from PVA film	K_H = 16.55; R^2 = 0.91	K = 0.523; R^2 = 0.98
Cu from PVA film	K_H = 13.38; R^2 = 0.83	K = 0.452; R^2 = 0.97
Zn from PVA sponge	K_H = 16.83; R^2 = 0.83	K = 0.302; R^2 = 0.91
Cu from PVA sponge	K_H = 17.67; R^2 = 0.86	K = 0.314; R^2 = 0.98
NE from PVA film	K_H = 13.74; R^2 = 0.73	K = 0.260; R^2 = 0.739
NE from PVA sponge	K_H = 15.64; R^2 = 0.66	K = 0.339; R^2 = 0.750

facilitated by water uptake and polymer chain relaxation. Upon hydration, the porous sponge structure and swollen film matrix create interconnected pathways that allow the gradual migration of nanoemulsion droplets toward the surrounding medium. The higher release from sponges can be attributed to their increased porosity and surface area, which enhance fluid penetration and diffusion rates. The Fickian diffusion behavior ($n < 0.45$) suggests minimal polymer erosion, indicating controlled release. Sustained liberation of NE maintains prolonged antimicrobial activity, thereby enhancing the therapeutic potency of the developed wound dressing system. A summary of Higuchi and KP model constants and fitted R^2 values is shown in Table 1. The fitted curves are shown in the SI (Fig. S3).

3.6. Biofunctional assays

3.6.1. Cell proliferation and collagen assay. Cell proliferation was quantified on days 1, 3, and 5 to evaluate whether the individual Bhasmas, NE or their combination could promote fibroblast and keratinocyte proliferation (Fig. 6 and 7). Representative images of cell proliferation and collagen assays are shown for day 3 in Fig. 6(a) and 7(a). On day 1, no significant difference was observed among groups, suggesting that the released bioactives were non-toxic and allowed normal cell attachment. By day 3, a significant increase in fibroblast and keratinocyte proliferation was seen in the TB, YB, and combined formulations (PVA TYN film and PVA TYN sponge) compared with the PVA control and untreated groups ($p <$ 0.01–0.001). By day 5, the combined systems, particularly the PVA TYN film, showed significantly greater proliferation in both cell lines compared with all other samples ($p < 0.0001$). These findings suggest that while TB and YB individually support cell growth, their synergistic effect with NE showed improved cell proliferation and metabolic activity. To further assess extracellular matrix (ECM) formation, Picrosirius Red staining was performed at day 3; representative images are shown in Fig. 6(a) and 7(a) (collagen panel). Cells treated with YB or TB alone indicated moderate collagen deposition, while a more pronounced effect was observed in the combined formulations, suggesting enhanced ECM remodelling. This shows that the *Yasad-Tamra*-NE combination in PVA leads to upregulated ECM-associated signalling, potentially through bioactive synergism between Cu^{2+} and Zn^{2+} ions that regulate fibroblast activity and collagen crosslinking enzymes, such as lysyl oxidase (LOX).[30] Phalloidin/DAPI staining (Fig. 6(a) and 7(a)) (Ki67 panel) further confirmed the influence of these materials on cytoskeletal organization and cell morphology. In all groups, actin filaments (red) were clearly visible, but cells cultured with PVATYN film and PVATYN sponge conditioned media exhibited highly organized, dense, and interconnected F-actin networks. The nuclei (blue) were uniformly distributed and more densely populated in these combined groups, indicating active spreading and proliferation. The cytoskeletal architecture in the PVATYN composites correlated strongly with the quantitative proliferation data, suggesting that the composite microenvironment supports cell adhesion, contractility, and mechanical communication with the matrix. The observed improvement in proliferation and ECM deposition can be attributed to the complementary biological roles of copper and zinc ions.

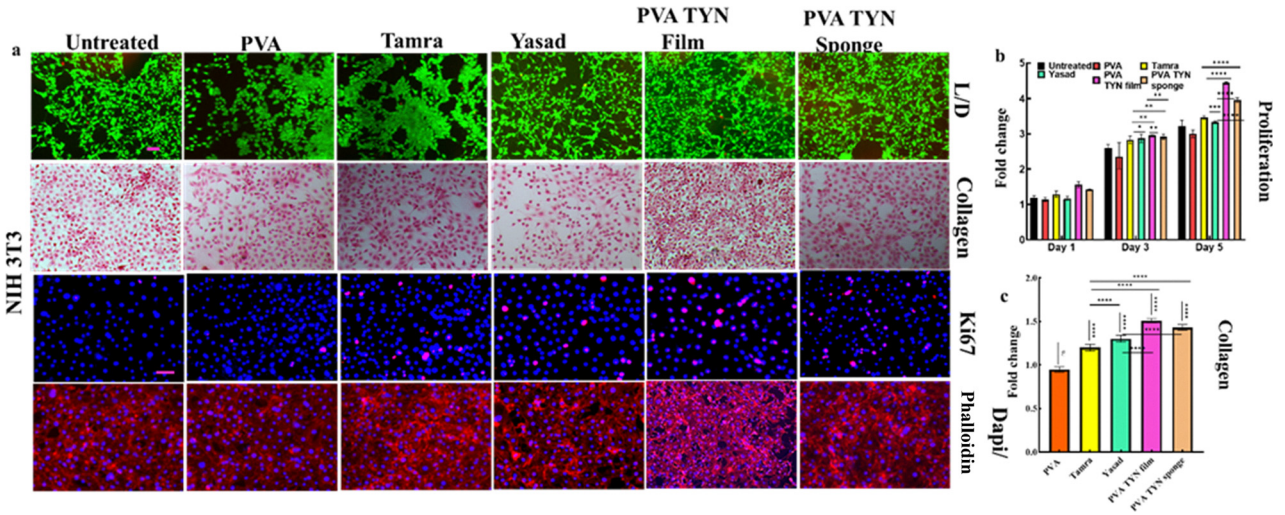

Fig. 6 Live/dead, cytoskeletal morphology, and proliferation of the fibroblasts and keratinocytes cultured on Tamra- and Yasad-based formulations. Representative fluorescent and bright-field images of the fibroblasts on day 3. Green: live cells (Calcein-AM); red: dead cells (PI); blue: nuclei (DAPI); and magenta: F-actin (phalloidin) (a). Quantitative Alamar Blue assay showing the time-dependent proliferation of the fibroblasts over 5 days (b). Quantitative collagen assay plot on day 3 (c). Both the PVATYN film and sponge groups exhibit significantly higher metabolic activity compared with the untreated control (*$p < 0.05$, **$p < 0.01$, and **$p < 0.001$). Data are presented as mean ± SD ($n = 3$). Mag 10 × scale bar 100 μm.

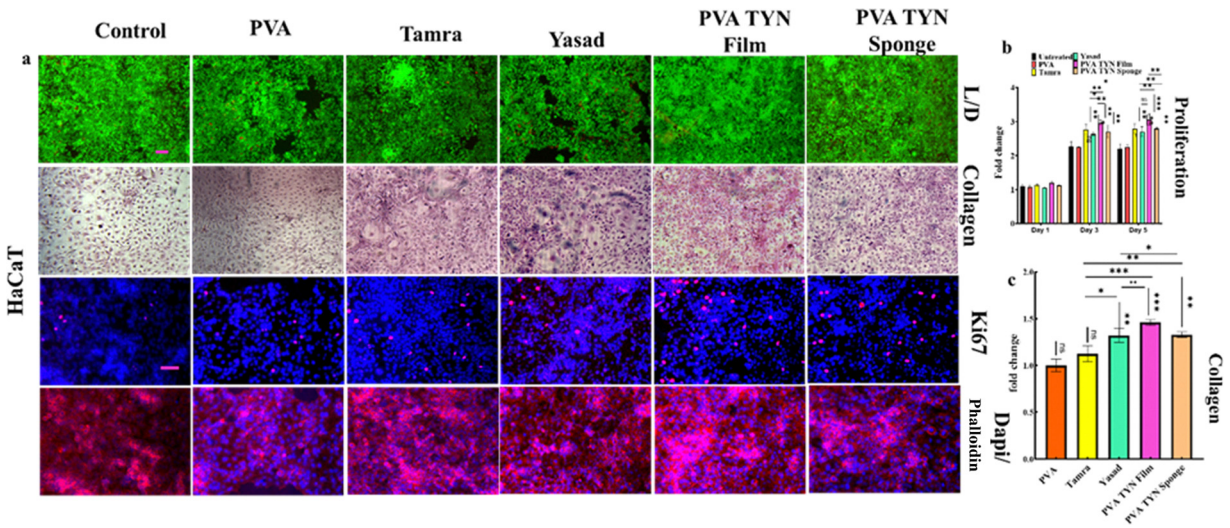

Fig. 7 Live/dead, cytoskeletal morphology, and proliferation of keratinocytes cultured on Tamra- and Yasad-based formulations. Representative fluorescent and bright-field images of on day 3. Green: live cells (Calcein-AM); red: dead cells (PI); blue: nuclei (DAPI); and magenta: F-actin (phalloidin) (a). Quantitative Alamar Blue assay showing time-dependent proliferation of the keratinocytes over 5 days (b). Quantitative collagen assay on day 3 (c). Both PVATYN film and sponge groups exhibit significantly higher metabolic activity compared with the untreated control (*$p < 0.05$, **$p < 0.01$, and **$p < 0.001$). Data are presented as mean ± SD ($n = 3$). Mag 10 × scale bar 100 μm.

Copper is a cofactor for fibroblast metabolic activity, while also catalysing collagen crosslinking *via* LOX.[31,32] Zinc, in contrast, regulates MMPs, TGF-β1, and DNA synthesis, which are essential for fibroblast proliferation and keratinocyte differentiation.[33,34] In addition, the presence of cinnamaldehyde NE is reported to show antioxidative protection and enhanced intracellular signalling through PI3K/Akt and MAPK pathways.[35,36] This may help to maintain redox balance, preventing oxidative-stress-induced senescence and promoting continuous proliferation.

3.6.2. Scratch assay. Scratch assays performed with both fibroblast and keratinocyte monolayers showed that all Bhasma-based formulations significantly enhanced cell migration compared to untreated controls (Fig. 8). In fibroblasts, untreated cells showed slow migration with 65% ± 3% wound closure after 48 h, while TB and YB alone yielded moderate improvement (83% ± 3% and 72% ± 4%, respectively). Incorporation of the Bhasmas with cinnamaldehyde NE in the PVATYN film and PVATYN sponge further accelerated fibroblast migration to 92% ± 2% and 87% ± 3%, respectively. A similar

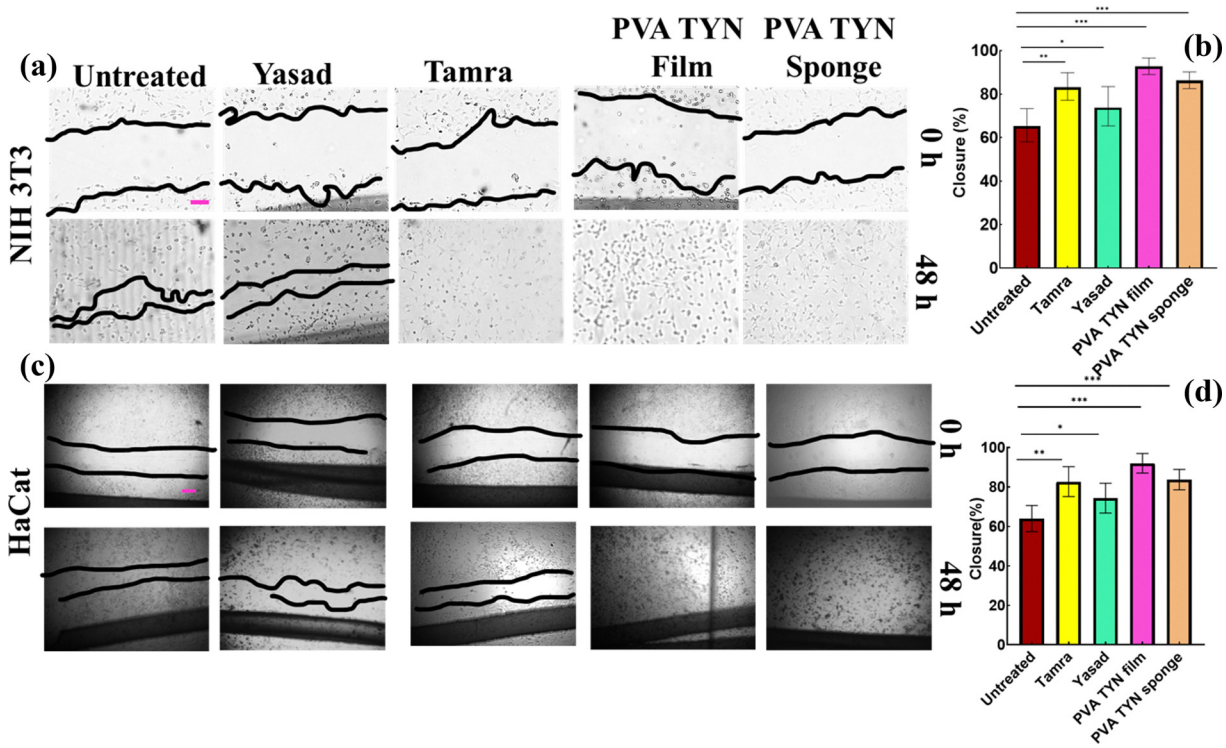

Fig. 8 Scratch assay (A). Representative phase-contrast micrographs illustrating the fibroblast migration at 0 h and 48 h post-scratch under different treatment conditions: untreated control, TB, YB, PVATYN film, and PVATYN sponge. The wound edges at each time point are marked by black lines. Mag 10 × scale bar 100 μm. (B). Quantitative analysis of the fibroblast wound-closure percentage after 48 h, showing significantly higher migration in the PVATYN film and sponge groups compared with the control ($p < 0.01$). (C) Representative scratch assay images of the keratinocytes at 0 h and 24 h for the same treatment groups. (D) Quantitative analysis of the keratinocyte closure percentage demonstrating enhanced re-epithelialization in PVA–TYN composites, with the film showing the greatest effect. Data represent mean ± SD ($n = 3$). Statistical significance: $p < 0.05$, *$p < 0.01$, and **$p < 0.001$ *vs.* untreated control. Mag 4 × scale bar 200 μm.

trend was seen for keratinocytes, where untreated monolayers showed only 62% ± 4% closure, while TB and YB produced 82% ± 3% and 75% ± 4% closure, respectively. The PVATYN film and PVATYN sponge again showed the highest rates, achieving 93% ± 2% and 89% ± 3% closure, respectively. The enhanced migration of both fibroblasts and keratinocytes seen with the PVATYN systems proves the synergistic bioactivity of Cu^{2+} and Zn^{2+} ions from TB and YB, together with cinnamaldehyde NE. Copper ions act as potent pro-migratory cofactors, activating ERK/MAPK signalling pathways that regulate actin reorganization and focal-adhesion turnover.[37–39] Zinc complements this effect by upregulating motility-critical integrins a2β1, a3β1, a6β4, and αvβ5, activating MMPs that clear ECM barriers.[40–45] Between the two material forms, the PVATYN film consistently outperformed the sponge in biochemical parameters, likely due to its moderate swelling ratio and ionic diffusion, which together facilitated better cellular functions. Comparable findings have been reported for Cu/Zn-doped hydrogels and bioactive-glass composites, which significantly enhanced fibroblast and keratinocyte migration and accelerated re-epithelialization *in vitro* and *in vivo*.[46,47]

3.6.3. Endothelial proliferation and angiogenesis. Copper is known to enhance endothelial proliferation, migration, and neo vessel formation.[48,49] Zinc regulates matrix metalloproteinases (MMP-2/-9), TGF-β1, and Smad signalling, contributing to endothelial survival, ECM remodelling, and angiogenic maturation.[50,51] Traditionally, TB and YB have long been recognized for their regenerative potential in Ayurvedic medicine, while cinnamaldehyde, the principal bioactive in cinnamon oil, is reported to activate PI3K/Akt and MAPK/ERK pathways to stimulate endothelial proliferation and angiogenesis.[52] Our results demonstrate that although TB alone exerts a positive effect on endothelial cell proliferation and angiogenic marker expression (VEGF), its combination with YB and cinnamaldehyde NE in the PVATYN film and sponges produces a markedly enhanced response Fig. 9. Live/Dead staining revealed predominantly green fluorescence in all groups, with elongated, spindle-like HUVEC morphology characteristic of healthy endothelium (Fig. 9(a)). Cells cultured with PVATYN film and PVATYN sponge conditioned media displayed greater spreading and cell connectivity compared with Tamra-only or untreated control. These observations align with the known effects of sustained Cu^{2+}/Zn^{2+} release on focal adhesion kinase (FAK) and MAPK/ERK activation, which regulate endothelial attachment and proliferation.[53–55] Quantitative analysis using Alamar Blue (Fig. 9(b)) showed a significant enhancement in HUVEC proliferation with the composite formulations. The PVATYN film exhibited the highest increase, followed by the PVA TYN sponge. These results suggest a synergistic proliferative effect from the co-release of Cu^{2+} and Zn^{2+} ions, consistent with

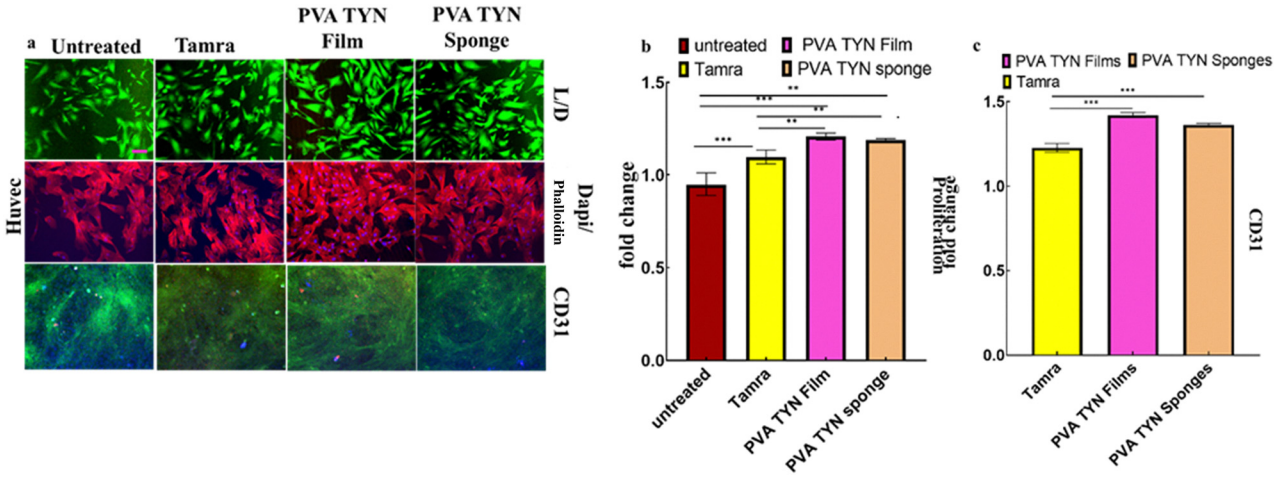

Fig. 9 Effect on endothelial cells. (a) Representative fluorescence micrographs of HUVECs on day 3, showing Live/dead staining (green: live cells and red: dead cells) and phalloidin/DAPI staining (red: F-actin and blue: nuclei). Cells on the PVATYN film and sponge showed enhanced spreading, dense cytoskeletal organization, and greater intercellular connectivity compared with Tamra alone or the control. Immunofluorescence staining of CD31 (green) showing prominent localization at cell–cell junctions in the cells cultured on PVATYN film and sponge, indicating enhanced endothelial differentiation and angiogenic phenotype maintenance. (b) Quantitative Alamar Blue assays showing a significant increase in HUVEC proliferation for the composite formulations on day 3. The PVATYN film group exhibited the highest fold change (1.32 ± 0.05), followed by the sponge (1.26 ± 0.04), relative to the untreated control ($p < 0.01$–0.001). (c) Quantitative analysis of the CD31 fluorescence intensity, demonstrating up to 1.45 ± 0.06-fold increase in the PVATYN film and 1.36 ± 0.05-fold in the sponge compared with Tamra alone ($p < 0.001$). Data represent mean ± SD ($n = 3$). Statistical significance: $p < 0.05$, *$p < 0.01$, and **$p < 0.001$ *vs.* control.

reports where copper stabilizes HIF-1α and induces VEGF secretion, while zinc promotes TGF-β/Smad-mediated growth and ECM synthesis.[30,56] In addition, cinnamaldehyde likely contributed antioxidant protection and mitigation of oxidative-stress-induced apoptosis. Immunofluorescence staining for CD31 (PECAM-1) further validated angiogenic differentiation (Fig. 9(a)). HUVECs cultured with PVATYN film and sponge conditioned media exhibited intense green fluorescence localized at cell junctions, indicative of endothelial connectivity. Quantitative analysis showed CD31 expression increased 1.45 ± 0.06-fold in the film and 1.36 ± 0.05-fold in the sponge compared with the Tamra group ($p < 0.001$). This elevated CD31 signal signifies enhanced intercellular junction formation and endothelial maturation, which are prerequisites for microvessel development. The effect likely stems from Cu^{2+}-induced HIF-1α/VEGF activation and Zn^{2+}-mediated ECM remodeling, which together create a pro-angiogenic niche. PVATYN film induced a slightly higher proliferation and CD31 expression than the sponge, likely due to a slower release rate.[57] Together, these findings establish that the PVATYN effectively supports endothelial proliferation and angiogenic phenotype maintenance as key prerequisites for vascularized tissue regeneration and accelerated wound healing.

3.6.4. Free radical scavenging and survival assays. The intracellular reactive oxygen species (ROS) levels were assessed using DCF-DA/PI staining after exposure to menadione, a superoxide generator, to evaluate the antioxidant capacity of the PVA TYN composites (Fig. 10). Menadione treatment markedly increased green fluorescence in the untreated group, indicating high intracellular ROS accumulation. In contrast, cells treated with extracts from Tamra and *Yasad Bhasma* showed visibly reduced fluorescence intensity, confirming partial mitigation of oxidative stress due to the redox-buffering action of released Cu^{2+} and Zn^{2+} ions. A further significant decrease in DCF fluorescence was observed in cells exposed to extracts from PVATYN film and PVATYN sponge, showing suppression of ROS generation. The film and sponge exhibited superior antioxidant protection relative to individual Bhasma extracts, suggesting a synergistic effect of the hybrid system combining metal ion release with the inherent radical-scavenging property of cinnamaldehyde in the NE. This elevated antioxidant activity is likely due to the gradual release of

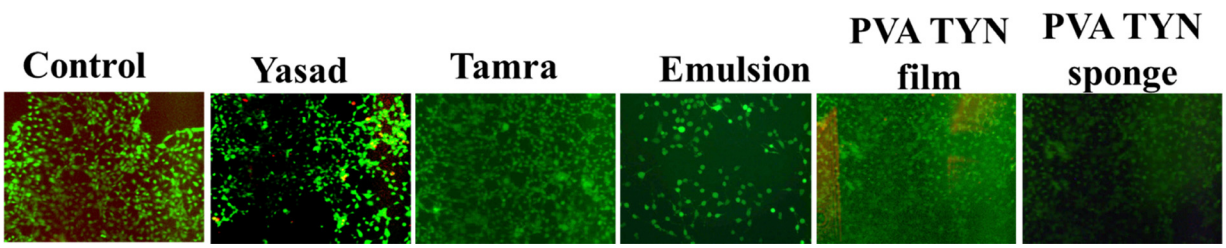

Fig. 10 DCF-DA/PI staining for the free-radical scavenging of different sample groups.

redox-active Cu^{2+}/Zn^{2+} ions that catalyse superoxide dismutation and cinnamaldehyde-mediated inhibition of NADPH oxidase-derived ROS, thereby attenuating menadione-induced oxidative stress.[58]

Overall, the *in vitro* studies project that Cu species primarily contribute to angiogenesis and antimicrobial action through redox cycling and ROS-mediated bacterial damage, while Zn phases regulate oxidative balance, enhance keratinocyte proliferation, and support tissue remodelling. This complementary ion activity explains the observed balance between antibacterial efficacy and cytocompatibility. NE release is governed by diffusion through the swollen PVA network and possible transient coordination with metal ions. Its anti-inflammatory and antibiofilm effects synergize with ion-mediated antimicrobial activity, while excessive phytochemical loading may modulate ion-release kinetics. Crosslinking density regulates release behavior, swelling enhances nutrient transport and cell migration, degradation governs the exposure of bioactive phases, and improved mechanical strength preserves scaffold integrity during healing.

In comparison, commercially available wound-healing hydrogels, such as DermaSyn®, Neoheal® Hydrogel, Restore Hydrogel, ActivHeal®, NU-GEL™, Purilon®, and Simpurity™ Hydrogel, primarily rely on hydrated polymeric networks (PEG, PVP, alginate, PVA, hyaluronic acid, or polyurethane) to maintain moisture balance and support autolytic healing. Most of these systems focus on hydration and exudate management rather than sustained antimicrobial delivery.[59] In contrast, the developed PVA-TYN film and sponge integrate inorganic bioactives (Tamra and *Yasad Bhasma*) with cinnamaldehyde nanoemulsion, enabling diffusion-controlled release alongside structural support. This multifunctional design aims to combine moisture retention, antimicrobial potency, and prolonged therapeutic action, thereby addressing limitations of conventional hydrogel dressings that lack controlled bioactive release.

4. Summary and conclusions

The present work demonstrates the synergistic wound-healing capability of *Tamra Bhasma* and *Yasad Bhasma* combined with cinnamaldehyde nanoemulsion within PVA-based hydrogel films and sponges. The developed formulations showed sustained, diffusion-controlled release of the bioactive components for over 24 h, supporting prolonged therapeutic action. Compared with conventional commercial hydrogels, such as NU-GEL™, Purilon®, Neoheal® Hydrogel, and Restore Hydrogel, which mainly provide moisture retention and passive protection, the PVA-TYN system offers multifunctional performance through controlled antimicrobial and antioxidant delivery. The composites exhibited strong free-radical scavenging (>80%) and bactericidal efficacy (>90%), highlighting improved infection control potential. Incorporation of Bhasma nanoparticles and nanoemulsion also enhanced the mechanical properties, improving the tensile behavior of the films and the compressive strength of the sponges, thereby overcoming the relatively weak mechanical stability often observed in highly hydrated commercial dressings. *In vitro* studies with NIH 3T3 fibroblasts and HaCaT keratinocytes demonstrated enhanced cell migration, proliferation, and angiogenic response compared to neat PVA controls, indicating improved regenerative performance. Overall, the indigenous PVA-TYN film and sponge present a multifunctional wound-dressing platform that integrates sustained bioactive release, antioxidant activity, antimicrobial potency, and mechanical robustness, suggesting strong potential for further *in vivo* evaluation and clinical translation in advanced wound-care applications.

Author contributions

Suhela Tyeb: conceptualization, methodology, and writing – original draft. Nitesh Kumar: data curation and resources. Vivek Verma: investigation and resources. Ashok Kumar: resources. Sanjana Koul: writing – reviewing and editing and supervision.

Conflicts of interest

There are no conflicts of interest to declare.

Data availability

The data supporting this article have been included as part of the supplementary information (SI). supplementary information: includes Fig. S1 and S2 showing the FTIR spectra of *Yasad Bhasma* and *Tamra Bhasma*, respectively, and Fig. S3 showing the fitting of the Higuchi models (left column) and KP models (right column) for the release kinetics of zinc, copper and the nanoemulsion. See DOI: https://doi.org/10.1039/d6ma00091f.

Acknowledgements

ST and SK would like to thank the Department of Biotechnology, Government of India, for funding the research work (DBT-RA/2023-24/call-I/RA/18). NK would like to acknowledge IIT Jammu for the characterization facilities, such as the SEM and FTIR instruments. ST would also like to thank Mr G. P Bajpai, Mr Pawan Kumar, the Department of Materials Science and Engineering and the Biosciences and Bioengineering Department, IIT Kanpur, for the laboratory facilities used for this work.

References

1 S. Tyeb, V. Verma and N. Kumar, Polysaccharide based transdermal patches for chronic wound healing: Recent advances and clinical perspective, *Carbohydr. Polym.*, 2023, **316**, 121038, DOI: 10.1016/j.carbpol.2023.121038.
2 H. Wang, Z. Xu, M. Zhao, G. Liu and J. Wu, Advances of hydrogel dressings in diabetic wounds, *Biomater. Sci.*, 2021, **9**, 1530–1546, DOI: 10.1039/d0bm01747g.
3 W. Zhang, L. Liu, H. Cheng, J. Zhu, X. Li, S. Ye and X. Li, Hydrogel-based dressings designed to facilitate wound

healing, *Mater. Adv.*, 2024, **5**, 1364–1394, DOI: 10.1039/D3MA00682D(accessed November 14, 2025).

4 X. Liang, H. J. Zhong, H. Ding, B. Yu, X. Ma, X. Liu, C. M. Chong and J. He, Polyvinyl Alcohol (PVA)-Based Hydrogels: Recent Progress in Fabrication, Properties, and Multifunctional Applications, *Polymers*, 2024, **16**(19), 2755, DOI: 10.3390/POLYM16192755.

5 W. Ji, M. Mizanur, R. Khan, M. Mahamudul and H. Rumon, Synthesis of PVA-Based Hydrogels for Biomedical Applications: Recent Trends and Advances, *Gels*, 2025, **11**, 88, DOI: 10.3390/GELS11020088.

6 K. Bialik-Wąs, K. Pluta, D. Malina, M. Barczewski, K. Malarz and A. Mrozek-Wilczkiewicz, Advanced SA/PVA-based hydrogel matrices with prolonged release of Aloe vera as promising wound dressings, *Mater. Sci. Eng. C*, 2021, **120**, 111667, DOI: 10.1016/j.msec.2020.111667.

7 L. Wang, Y. Yu, X. Zhao, Z. Zhang, X. Yuan, J. Cao, W. Meng, L. Ye, W. Lin and G. Wang, A Biocompatible Self-Powered Piezoelectric Poly(vinyl alcohol)-Based Hydrogel for Diabetic Wound Repair, *ACS Appl. Mater. Interfaces*, 2022, **14**, 46273–46289, DOI: 10.1021/ACSAMI.2C13026.

8 Z. Wang, S. Gao, W. Zhang, H. Gong, K. Xu, C. Luo, W. Zhi, X. Chen, J. Li and J. Weng, Polyvinyl alcohol/chitosan composite hydrogels with sustained release of traditional Tibetan medicine for promoting chronic diabetic wound healing, *Biomater. Sci.*, 2021, **9**, 3821–3829, DOI: 10.1039/D1BM00346A.

9 F. Ciftci, A. C. Özarslan and N. Evcimen Duygulu, Production and comprehensive characterization of PVA/chitosan transdermal composite mats loaded with bioactive curcumin; evaluation of its release kinetics, antioxidant, antimicrobial, and biocompatibility features, *J. Appl. Polym. Sci.*, 2024, **141**, e55874, DOI: 10.1002/APP.55874.

10 N. Rashid, S. H. Khalid, I. Ullah Khan, Z. Chauhdary, H. Mahmood, A. Saleem, M. Umair and S. Asghar, Curcumin-Loaded Bioactive Polymer Composite Film of PVA/Gelatin/Tannic Acid Downregulates the Pro-inflammatory Cytokines to Expedite Healing of Full-Thickness Wounds, *ACS Omega*, 2023, **8**, 7575–7586, DOI: 10.1021/ACSOMEGA.2C07018.

11 N. Pattanaik, A. V. Singh, R. S. Pandey, B. K. Singh, M. Kumar, S. K. Dixit and Y. B. Tripathi, Toxicology and free radicals scavenging property of *Tamra bhasma*, *Indian J. Clin. Biochem.*, 2003, **18**, 181, DOI: 10.1007/BF02867385.

12 P. S. Bafna and S. D. Patil, Physicochemical characterisation and anti-inflammatory activity of ayurvedic herbo-metallic *Tamra bhasma* in acute and chronic models of inflammation, *Mater. Technol.*, 2018, **33**(10), 681–688, DOI: 10.1080/10667857.2018.1494241.

13 S. Honwad, T. S. Bairy, M. Ravi and B. Ravishankar, Hepatoprotective activity of Somanathi *Tamra Bhasma* in paracetamol induced liver toxicity in albino- rats, *J. Phytopharmacol.*, 2015, **4**, 143–146, DOI: 10.31254/PHYTO.2015.4303.

14 P. S. Bafna and S. D. Patil, Physicochemical characterisation and anti-inflammatory activity of ayurvedic herbo-metallic *Tamra bhasma* in acute and chronic models of inflammation, *Mater. Technol.*, 2018, **33**, 681–688, DOI: 10.1080/10667857.2018.1494241.

15 R. K. Singh, S. Kumar, A. K. Aman, S. M. Karim, S. Kumar and M. Kar, Study on physical properties of Ayurvedic nanocrystalline *Tamra Bhasma* by employing modern scientific tools, *J. Ayurveda Integr. Med.*, 2019, **10**, 88–93, DOI: 10.1016/j.jaim.2017.06.012.

16 D. Durgalakshmi, R. Ajay Rakkesh, T. Bhargavi Ram and S. Balakumar, Comparative studies on Indian traditional nanomedicine Yashadha Bhasma and zinc oxide nanoparticles for anti-diabetic activity, *Mater. Res. Express*, 2017, **4**, 075016, DOI: 10.1088/2053-1591/AA7A26.

17 A. Pareek and N. Bhatnagar, Physico-chemical characterization of traditionally prepared Yashada bhasma, *J. Ayurveda Integr. Med.*, 2020, **11**, 228–235, DOI: 10.1016/j.jaim.2018.11.004.

18 A. K. Suresh and S. G. Kane, *Physiochemical and Biological studies of Jasada Bhasma, a herbo-mineral Indian Traditional Medicine*, 2008.

19 C. Shu, L. Ge, Z. Li, B. Chen, S. Liao, L. Lu, Q. Wu, X. Jiang, Y. An, Z. Wang and M. Qu, Antibacterial activity of cinnamon essential oil and its main component of cinnamaldehyde and the underlying mechanism, *Front. Pharmacol.*, 2024, **15**, 1378434, DOI: 10.3389/FPHAR.2024.1378434/BIBTEX.

20 S. G. Seyed Ahmadi, M. R. Farahpour and H. Hamishehkar, Topical application of Cinnamon verum essential oil accelerates infected wound healing process by increasing tissue antioxidant capacity and keratin biosynthesis, *Kaohsiung J. Med. Sci.*, 2019, **35**, 686–694, DOI: 10.1002/KJM2.12120.

21 H. Moustafa, H. E. Nasr and A. M. Youssef, Development of antibacterial carboxymethyl cellulose/quaternized starch bionanocomposites based on cinnamon essential oil nanoemulsion for wound healing applications, *Biomass Convers. Biorefin.*, 2024, **14**, 27477–27489, DOI: 10.1007/S13399-022-03403-2/TABLES/2.

22 S. Tyeb, P. A. Shiekh, V. Verma and A. Kumar, Adipose-Derived Stem Cells (ADSCs) Loaded Gelatin-Sericin-Laminin Cryogels for Tissue Regeneration in Diabetic Wounds, *Biomacromolecules*, 2020, **21**, 294–304, DOI: 10.1021/acs.biomac.9b01355.

23 A. Dhillon, S. Sardana and A. R. Thakkar, Development and Validation of HPLC and UV Spectrophotometric Method for the Quantification of Cinnamaldehyde in Cinnamon Bark Extract, *J. Nat. Rem.*, 2023, **23**, 111–119, DOI: 10.18311/JNR/2023/30836.

24 S. Tyeb, N. Kumar, A. Kumar and V. Verma, Flexible agar-sericin hydrogel film dressing for chronic wounds, *Carbohy. Polym.*, 2018, **200**, 572–582, DOI: 10.1016/j.carbpol.2018.08.030.

25 J. Stephen-Haynes, Exudate management to promote healing, *Nursing and Residential Care*, 2015, **17**, 322–326, DOI: 10.12968/NREC.2015.17.6.322.

26 A. Punjataewakupt and P. Aramwit, Wound dressing adherence: a review, *J. Wound Care*, 2022, **31**, 406–423, DOI: 10.12968/JOWC.2022.31.5.406.

27 Y. Herdiana, N. Wathoni, S. Shamsuddin and M. Muchtaridi, Drug release study of the chitosan-based nanoparticles, *Heliyon*, 2022, **8**, e08674, DOI: 10.1016/j.heliyon.2021.e08674.
28 M. Mojahedi, P. Heydari and A. Z. Kharazi, Preparation and characterization of an antibacterial CMC/PCL hydrogel films containing CIP/Cur: In vitro and in vivo evaluation of wound healing activity, *Int. J. Biol. Macromol.*, 2024, **282**, 136570, DOI: 10.1016/j.ijbiomac.2024.136570.
29 J. Emami, N. Mostolizadeh, M. Tabbakhian, P. Heydari, A. Z. Kharazi, M. Minaeiyan, F. Hasanzadeh, M. Mirian and A. Talebi, Development and evaluation of gelatin/hyaluronic acid nanofibrous dressing loaded with silver nanoparticles and phenytoin for enhanced wound healing: an in-vitro and in-vivo study, *Res. Pharm. Sci.*, 2025, **20**, 610, DOI: 10.4103/rps.rps_60_25.
30 N. K. R. Gadaime, R. B. Rabiatul, G. A. Govindasamy, Y. Bustami and S. Sreekantan, Advanced Hydrogel Dressing with Zinc Oxide-Copper Oxide Nanocomposite for Effective Wound Management: Mechanochemistry, Antibacterial Efficacy, Cytocompatibility and Wound Healing Potentials, *J. Polym. Environ.*, 2025, **33**, 1601–1614, DOI: 10.1007/S10924-024-03468-2.
31 Y. Yang Niu, Y. Ying Zhang, Z. Zhu, X. Qin Zhang, X. Liu, S. Ya Zhu, Y. Song, X. Jin, B. Lindholm and C. Yu, Elevated intracellular copper contributes a unique role to kidney fibrosis by lysyl oxidase mediated matrix crosslinking, *Cell Death Dis.*, 2020, **11**, 211, DOI: 10.1038/S41419-020-2404-5.
32 G. Borkow, Using Copper to Improve the Well-Being of the Skin, *Curr. Chem. Biol.*, 2014, **8**, 89, DOI: 10.2174/2212796809666150227223857.
33 Y. Qiu, Y. Gao, D. Yu, L. Zhong, W. Cai, J. Ji, F. Geng, G. Tang, H. Zhang, J. Cao, J. Zhang and S. Zhang, Genome-Wide Analysis Reveals Zinc Transporter ZIP9 Regulated by DNA Methylation Promotes Radiation-Induced Skin Fibrosis via the TGF-β Signaling Pathway, *J. Invest. Dermatol.*, 2020, **140**, 94–102.e7, DOI: 10.1016/j.jid.2019.04.027.
34 D. Beyersmann and H. Haase, Functions of zinc in signaling, proliferation and differentiation of mammalian cells, *Biometals*, 2001, **14**, 331–341, DOI: 10.1023/A:1012905406548.
35 X. Yuan, L. Han, P. Fu, H. Zeng, C. Lv, W. Chang, R. S. Runyon, M. Ishii, L. Han, K. Liu, T. Fan, W. Zhang and R. Liu, Cinnamaldehyde accelerates wound healing by promoting angiogenesis via up-regulation of PI3K and MAPK signaling pathways, *Lab. Invest.*, 2018, **98**, 783–793, DOI: 10.1038/s41374-018-0025-8.
36 J. Sankaranarayanan, S. C. Lee, H. K. Kim, J. Y. Kang, S. S. Kuppa and J. K. Seon, Cinnamaldehyde-Mediated Suppression of MMP-13, COX-2, and IL-6 Through MAPK and NF-κB Signaling Inhibition in Chondrocytes and Synoviocytes Under Inflammatory Conditions, *Int. J. Mol. Sci.*, 2024, **25**, 12914, DOI: 10.3390/IJMS252312914.
37 W. Feng, F. Ye, W. Xue, Z. Zhou and Y. J. Kang, Copper Regulation of Hypoxia-Inducible Factor-1 Activity, *Mol. Pharmacol.*, 2008, **75**, 174, DOI: 10.1124/MOL.108.051516.
38 D. C. Rigiracciolo, A. Scarpelli, R. Lappano, A. Pisano, M. F. Santolla, P. De Marco, F. Cirillo, A. R. Cappello, V. Dolce, A. Belfiore, M. Maggiolini and E. M. De Francesco, Copper activates HIF-1α/GPER/VEGF signalling in cancer cells, *Oncotarget*, 2015, **6**, 34158, DOI: 10.18632/ONCOTARGET.5779.
39 I. Tenaud, S. Leroy, N. Chebassier and B. Dreno, Zinc, copper and manganese enhanced keratinocyte migration through a functional modulation of keratinocyte integrins, *Exp. Dermatol.*, 2000, **9**, 407–416, DOI: 10.1034/J.1600-0625.2000.009006407.x.
40 A. B. G. Lansdown, U. Mirastschijski, N. Stubbs, E. Scanlon and M. S. Ågren, Zinc in wound healing: Theoretical, experimental, and clinical aspects, *Wound Repair Regen.*, 2007, **15**, 2–16, DOI: 10.1111/j.1524-475x.2006.00179.x.
41 R. Nosrati, S. Kheirouri, R. Ghodsi and H. Ojaghi, The effects of zinc treatment on matrix metalloproteinases: A systematic review, *J. Trace Elem. Med. Biol.*, 2019, **56**, 107–115, DOI: 10.1016/j.jtemb.2019.08.001.
42 R. Nosrati, S. Kheirouri, R. Ghodsi and H. Ojaghi, The effects of zinc treatment on matrix metalloproteinases: A systematic review, *J. Trace Elem. Med. Biol.*, 2019, **56**, 107–115, DOI: 10.1016/j.jtemb.2019.08.001.
43 H. Sharir, A. Zinger, A. Nevo, I. Sekler and M. Hershfinkel, Zinc Released from Injured Cells Is Acting via the Zn2 + -sensing Receptor, ZnR, to Trigger Signaling Leading to Epithelial Repair, *J. Biol. Chem.*, 2010, **285**, 26097, DOI: 10.1074/jbc.m110.107490.
44 P. H. Lin, M. Sermersheim, H. Li, P. H. U. Lee, S. M. Steinberg and J. Ma, Zinc in Wound Healing Modulation, *Nutrients*, 2017, **10**, 16, DOI: 10.3390/NU10010016.
45 A. B. G. Lansdown, U. Mirastschijski, N. Stubbs, E. Scanlon and M. S. Ågren, Zinc in wound healing: Theoretical, experimental, and clinical aspects, *Wound Repair Regen.*, 2007, **15**, 2–16, DOI: 10.1111/J.1524-475x.2006.00179.x.
46 F. Kermani, S. Nazarnezhad, Z. Mollaei, S. Mollazadeh, A. Ebrahimzadeh-Bideskan, V. R. Askari, R. K. Oskuee, A. Moradi, S. A. Hosseini, Z. Azari, F. Baino and S. Kargozar, Zinc- and Copper-Doped Mesoporous Borate Bioactive Glasses: Promising Additives for Potential Use in Skin Wound Healing Applications, *Int. J. Mol. Sci.*, 2023, **24**, 1304, DOI: 10.3390/IJMS24021304.
47 B. M. Elmowafy, R. M. Ramadan, A. R. Ghazy, I. S. Fahim, T. M. Meaz, R. Ghazy and A. M. Abdelghany, Effect of copper and zinc oxide doping in 13–93B3 borate glass for enhanced wound healing, *Ceram. Int.*, 2025, **51**, 34650–34662, DOI: 10.1016/j.ceramint.2025.05.188.
48 D. C. Rigiracciolo, A. Scarpelli, R. Lappano, A. Pisano, M. F. Santolla, P. De Marco, F. Cirillo, A. R. Cappello, V. Dolce, A. Belfiore, M. Maggiolini and E. M. De Francesco, Copper activates HIF-1α/GPER/VEGF signalling in cancer cells, *Oncotarget*, 2015, **6**, 34158, DOI: 10.18632/oncotarget.5779.
49 E. Bosch-Rué, L. Díez-Tercero, R. Rodríguez-Gonzá lez, B. M. Bosch-Canals and R. A. Perez, Assessing the potential role of copper and cobalt in stimulating angiogenesis for

tissue regeneration, *PLoS One*, 2021, **16**, e0259125, DOI: 10.1371/journal.pone.0259125.

50 J. Zhao, J. Du, Y. Zheng, Y. Fang, J. Huang, J. Wu, Y. Wu and T. Nie, Zinc ions coordinated carboxymethyl chitosan hydrogel doped with ellagic acid for accelerative diabetic wound healing, *Int. J. Biol. Macromol.*, 2025, **327**, 147372, DOI: 10.1016/j.ijbiomac.2025.147372.

51 C. Zhao, J. Yang, W. Chen, C. Lu, Z. Zeng, T. Jiang and W. Liu, Gelatin/Dopamine/Zinc-Doped Ceria/Curcumin nanocomposite hydrogels for repair of chronic refractory wounds, *Int. J. Pharm.*, 2024, **663**, 124575, DOI: 10.1016/j.ijpharm.2024.124575.

52 X. Yuan, L. Han, P. Fu, H. Zeng, C. Lv, W. Chang, R. S. Runyon, M. Ishii, L. Han, K. Liu, T. Fan, W. Zhang and R. Liu, Cinnamaldehyde accelerates wound healing by promoting angiogenesis via up-regulation of PI3K and MAPK signaling pathways, *Lab. Invest.*, 2018, **98**, 783–798, DOI: 10.1038/S41374-018-0025-8.

53 D. Liang, M. Yang, B. Guo, J. Cao, L. Yang, X. Guo, Y. Li and Z. Gao, Zinc Inhibits H2O2-Induced MC3T3-E1 Cells Apoptosis via MAPK and PI3K/AKT Pathways, *Biol. Trace Elem. Res.*, 2012, **148**(3), 420–429, DOI: 10.1007/S12011-012-9387-8.

54 Y. Luo, H. Zhang, Z. Wang, J. Jiao, Y. Wang, W. Jiang, T. Yu, H. Liu, L. Guan, M. Li and M. Wu, Strategic incorporation of metal ions in bone regenerative scaffolds: multifunctional platforms for advancing osteogenesis, *Regen. Biomater.*, 2025, **12**, rbaf068, DOI: 10.1093/RB/RBAF068.

55 E. Urso and M. Maffia, Behind the Link between Copper and Angiogenesis: Established Mechanisms and an Overview on the Role of Vascular Copper Transport Systems, *J. Vasc. Res.*, 2016, **52**, 172–196, DOI: 10.1159/000438485.

56 Q. Wang, Q. Li, L. Zhu, C. Lin, Q. Chen and H. Chen, Fabrication of Cu/ZnO-loaded chitosan hydrogel for an effective wound dressing material to advanced wound care and healing efficiency after caesarean section surgery, *Int. Wound J*, 2024, **21**, e14366, DOI: 10.1111/IWJ.14366.

57 J. C. Palmaz, A. Benson and E. A. Sprague, Influence of surface topography on endothelialization of intravascular metallic material, *J. Vasc. Interv. Radiol.*, 1999, **10**, 439–444, DOI: 10.1016/S1051-0443(99)70063-1.

58 A. V. Kozlov, S. Javadov and N. Sommer, Cellular ROS and Antioxidants: Physiological and Pathological Role, *Antioxidants*, 2024, **13**, 602, DOI: 10.3390/ANTIOX13050602.

59 V. Gounden and M. Singh, Hydrogels and Wound Healing: Current and Future Prospects, *Gels*, 2024, **10**, 43, DOI: 10.3390/gels10010043.